ELSEVIER

Contents lists available at ScienceDirect

# Additive Manufacturing

journal homepage: www.elsevier.com/locate/addma



# Effects of laser-energy density and build orientation on the structure–property relationships in as-built Inconel 718 manufactured by laser powder bed fusion



Dillon S. Watring<sup>a</sup>, Jake T. Benzing<sup>b</sup>, Nikolas Hrabe<sup>b</sup>, Ashley D. Spear<sup>a,\*</sup>

- <sup>a</sup> Department of Mechanical Engineering, University of Utah, Salt Lake City, UT, USA
- <sup>b</sup> National Institute of Standards and Technology (NIST), Boulder, CO, USA

#### ARTICLE INFO

Keywords:
Laser powder bed fusion
Inconel 718
Microstructure
Defects
Porosity
Tensile properties
Characterization

#### ABSTRACT

This study investigates the effects of build orientation and laser-energy density on the pore structure, microstructure, and tensile properties of Inconel 718 manufactured by laser powder bed fusion. Three different build conditions were selected for comparison based on previous research (namely, the conditions that resulted in the worst and best fatigue lifetimes):  $0^{\circ}$  build orientation and  $38\,\mathrm{J/mm^3}$  laser-energy density,  $0^{\circ}$  build orientation and  $62\,\mathrm{J/mm^3}$  laser-energy density. Differences in porosity were measured between each build condition. In terms of microstructure, all three conditions exhibited a predominantly <001> texture in the build direction, grains elongated in the build direction, and a sub-grain structure oriented with the build direction that consisted of dislocation networks decorated with nano-scale precipitates. Build orientation  $(0^{\circ}$  versus  $60^{\circ}$  with respect to the build plate) produced a difference in yield strength due to anisotropic grain morphology and effective grain size. The low laser-energy density specimens showed a significant decrease in all mechanical properties compared to the high laser-energy density specimens because the amount (6.91% by volume) and size of the lack-of-fusion porosity (from insufficient melting) surpassed a level at which microstructure (the grain and sub-grain structure) no longer governs quasi-static mechanical properties. This work provides insight that could enable the tunability of structure-property relationships in as-built Inconel 718 by optimizing laser-energy density and build orientation.

# 1. Introduction

Nickel-based superalloys have become increasingly popular in the aerospace, nuclear, and marine industries [1,2]. Specifically, one nickel-based superalloy, Inconel, has become an alloy of choice in many applications due in part to its ability to retain high strength over a wide range of temperatures [3]. Inconel 718 (IN718), one of the most commonly used Inconel alloys, is a Ni–Cr–Fe austenitic superalloy, which has excellent mechanical properties especially at high temperatures and in corrosive environments [4]. A passivating oxide layer is created during the heating of Inconel, which provides some thermal insulation and corrosion resistance, leading to a maintained strength at high temperatures [5]. IN718 consists of a  $\gamma$ -fcc phase, known as the  $\gamma$ -matrix, that is rich in Ni, Cr, and Fe [6]. IN718 is also a precipitation-strengthened superalloy with the main strengthening phases being the  $\gamma$ -fcc and  $\gamma$ "-bct phases, which consist of Ni<sub>3</sub>(Al,Ti,Nb) and Ni<sub>3</sub>Nb,

respectively. The  $\gamma''$ -bct phase exhibits a higher degree of strengthening than the  $\gamma'$ -fcc phase, but the  $\gamma''$ -bct phase metastability can lead to additional phases such as carbides,  $\delta$  precipitates, and Laves phases. Traditionally, IN718 has been used in wrought, cast, and powder metallurgy applications with great success. However, the high hardness and low thermal conductivity of IN718 make it difficult and costly to machine [7–9], which leads to tool over-wear and poor surface integrity of the finished part [10]. Additive manufacturing techniques, which can create near-net shaped parts, could be a solution to some of the machining concerns associated with IN718.

Additive manufacturing (AM) has quickly become a popular tool in a variety of different industries [11–13]. Some of the benefits of AM techniques over traditional manufacturing include the ability to achieve high accuracy in fine details, reduced manufacturing time, and the ability to use a variety of metals and their alloys [14]. One of the most commonly used AM processes is laser powder bed fusion (L-PBF<sup>1</sup>)

<sup>\*</sup> Corresponding author.

E-mail address: ashley.spear@utah.edu (A.D. Spear).

<sup>&</sup>lt;sup>1</sup> Many of the works referenced throughout this manuscript use the terms selective laser melting (SLM) or direct metal laser sintering (DMLS); however, to be consistent with ASTM standards, these terms have been replaced by L-PBF in this manuscript.

[15,16]. In this method, metal powder is first spread or rolled onto a build plate. A scanning laser is used to locally melt/fuse a thin layer of the metal powder. This is repeated layer-by-layer to create a three-dimensional solid structure [14]. Although AM techniques address many concerns and issues associated with machining IN718 [17], challenges still arise during the L-PBF process, including variations in NbC fractions and porosity with respect to build height [18].

There has been a large amount of research done investigating the porosity in L-PBF metals (e.g., [19–22]). For example, it has been found that varying laser-energy density leads to differences in the porosity and fatigue life of L-PBF IN718 [23]. Pores in AM components are typically classified into three main categories: gas pores, keyhole pores, and lack-of-fusion (LOF) pores [24]. While hot isostatic pressing (HIP) can significantly decrease porosity in AM builds [25–27], HIP requires an application of high heat and pressure, which may not be possible in certain situations, depending on the size of the component or availability of such equipment in field applications.

The microstructure of IN718 manufactured by L-PBF also presents a challenge in deciphering processing-structure-property relationships. The typical microstructure of as-built L-PBF IN718 consists of grains with an anisotropic morphology. However, there has been little work investigating the variation of the as-built microstructure due to varying processing parameters. Additionally, dendritic sub-grain structures that are slender and uniformly distributed have been observed in the microstructure. These sub-grain structures have been shown to exist in metal alloys produced by laser-based manufacturing, and their characteristics can vary depending on the applied laser-energy density [28,29]. Moreover, previous work has shown that for L-PBF stainless steels, the sub-grain structures showed a strengthening effect [30,31]. While carbides and oxides reside along the sub-grain boundaries (mainly from Nb segregation during the L-PBF process) [32], the main strengthening phases of IN718 ( $\gamma'$ -fcc and  $\gamma''$ -bct) are usually produced after appropriate heat treatment and slow cooling [33,34]. However, when standard heat treatments are applied to L-PBF IN718, unwanted phases can precipitate (the  $\delta$  phase in particular) and negatively impact mechanical properties [35-37]. Also, traditional heat treatments tend to completely erase the elongated grain morphology and the sub-grain structures. Recent research efforts have focused on tailoring heat treatments to retain the sub-grain structures in AM IN718 [32] since the sub-grain structures in L-PBF IN718 exhibit a positive impact on creep resistance [38]. Another example of maintaining elongated grain morphology includes the work from Amato et al. [25], which showed that a specific HIP treatment of L-PBF IN718 still produced grains elongated in the build direction, plus a large amount of  $\gamma'$  and  $\gamma''$ .

Previous work by the authors showed that laser-energy density and build orientation had a significant influence on the high-cycle fatigue life of as-built L-PBF IN718 [39]. However, there was no investigation into the influence of the laser-energy density and build orientation on the variability of the three-dimensional pore structure and microstructure. Therefore, build conditions were selected from the previous work [39] to investigate the extreme cases of fatigue (i.e., the highest and lowest fatigue lifetimes) while considering differences in laser-energy density and build orientation. The objective of this study is to quantify the three-dimensional pore structure, microstructure, and quasi-static tensile properties for three different build conditions selected among the previously tested conditions [39]: 0° build orientation and 38 J/mm<sup>3</sup> laser-energy density (the absolute lowest fatigue life), 0° build orientation and 62 J/mm<sup>3</sup> laser-energy density (the lowest fatigue life for that specific laser-energy density and the highest fatigue life for that specific build orientation), and 60° build orientation and 62 J/mm<sup>3</sup> laser-energy density (the absolute greatest fatigue life). Although there have been previous investigations of microstructure and pore structure in L-PBF IN718, few studies exist in the open literature that have investigated the material in the as-built condition (without heat treatments or stress relieving) and the corresponding variability of the pore structure, microstructure, and tensile properties. However, the as-built condition of L-PBF IN718 is an important condition to study due to potential applications, such as deployment of AM machines in the field, where it may not be possible to perform heat treatments. Furthermore, the as-built condition contains two potentially advantageous and unique microstructural features. First, there is a lack of the deleterious  $\delta$  phase that is commonly found in the stress-relieved condition. Second, the as-built condition contains a sub-grain structure that has been shown to benefit mechanical behavior in other AM material systems, and this sub-grain structure is eliminated during homogenization heat treatments. Thus, to better optimize AM parts for use in such applications, there is a need to better understand the relationships among laser-energy density, build orientation, pore structure, microstructure, and tensile properties for the as-built condition.

#### 2. Material and methods

#### 2.1. Build parameters and tension testing

In this study, three build conditions were selected among 25 candidate build conditions that were examined previously by the authors [39], in which ASTM E466-15 standard fatigue specimens [40] were fabricated using a 3D Systems<sup>2</sup> ProX DMP 320 machine and IN718 powder. The entire build plate from the previous work is shown in Fig. 1a. The three build conditions were selected that resulted in the extreme cases of fatigue life and also exhibited variability in the build orientation and laser-energy density. The laser-energy density can be calculated by  $E_{\rho} = \frac{P}{v \, \text{hr}}$ , where *P* is the laser power, *v* is the scan speed, *h* is the hatch spacing, and t is the layer thickness [41]. The values of the laser power and scan speed of the three build conditions are provided in Table 1. Build orientation is reported with respect to the build plate. The first build condition had a 0° build orientation and a 38 J/mm<sup>3</sup> laser-energy density. The second build condition had a 0° build orientation and a 62 J/mm3. The final build condition had a 60° build orientation and a 62 J/mm3 laser-energy density. For all three conditions, the layer thickness (30 µm) and hatch spacing (100 µm) were held constant using standard values.

Grip sections of nine specimens, which were tested in the previous work [39], were used in this study. Each grip section was thinned from 3.18 to 1 mm (Fig. 1c) using wire electrical discharge machining (wire-EDM). Four tensile specimens were excised from each of the 1 mm-thick wafers using wire-EDM (target dimensions provided in Fig. 1d). Twelve tensile specimens were extracted for each build condition (36 total). However, four specimens were lost from the third build condition due to non-optimized settings on the first attempt with the wire-EDM process, so a total of 32 tensile specimens were available for this study. The tensile specimens were loaded to failure in uniaxial tension at a strain rate of  $1 \times 10^{-3} \,\mathrm{s}^{-1}$ . The linear portion of the stress-strain curve was fit in accordance with ASTM E3076-18 [42] to calculate Young's modulus. The other tensile properties (yield strength, ultimate tensile strength, uniform elongation, and elongation at fracture) were found according to practices recommended in ASTM E8-16a [43]. An analysis of variance (ANOVA) was completed with InStat software and used to test the null hypotheses that the tensile properties were equal across the three build conditions; significance is defined as p < 0.01.

# 2.2. X-ray computed tomography and electron microscopy

Prior to tensile testing, one specimen from each build condition was

<sup>&</sup>lt;sup>2</sup> Certain commercial software, equipment, instruments or materials are identified in this paper to adequately specify the experimental procedure. Such identification is not intended to imply recommendation or endorsement by the National Institute of Standards and Technology, nor is it intended to imply that the equipment or materials identified are necessarily the best available for the purpose.

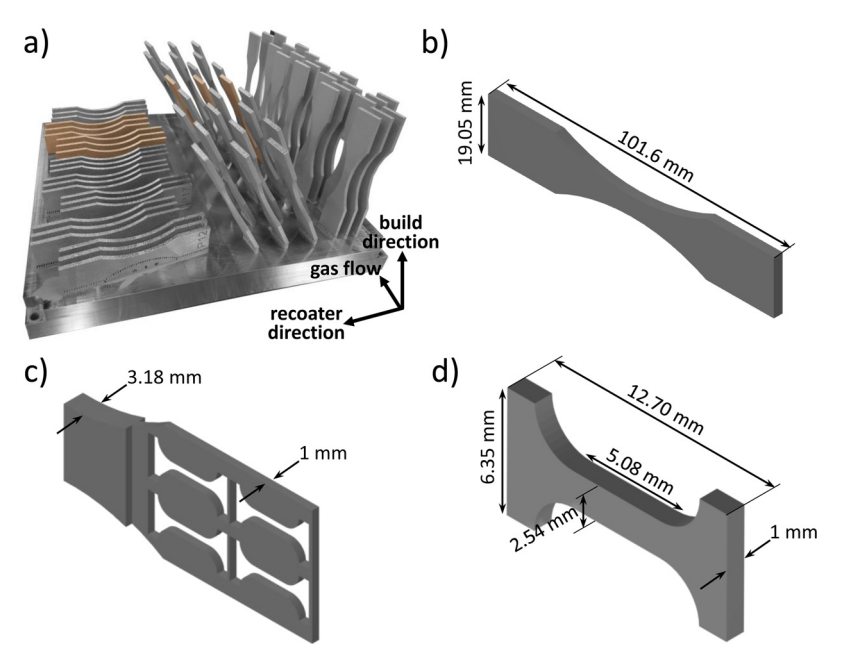


**Fig. 1.** Reuse of fatigue specimens from a previous study [39] to perform detailed materials characterization and miniaturized tensile testing in the current study. (a) All as-built IN718 fatigue specimens on the build plate prior to removal (from [39]); the nine specimens used in the current study are highlighted (refer to electronic version for color distinction). (b) Target dimensions for the fatigue specimens in accordance with ASTM E466-15. (c) The thinned grip region of the fatigue specimens, from which the tensile specimens are excised. (d) The tensile specimen target dimensions.

Table 1
L-PBF IN718 processing parameters for the three build conditions.

Build condition	Laser power (W)	Scan speed (mm/s)	Layer thickness (µm)	Build orientation (°)	Laser- energy density (J/mm³)
1	168	1475	30	0	38
2	330	1770	30	0	62
3	220	1180	30	60	62

analyzed in the gauge region to characterize potential differences in the three-dimensional pore structures. A Zeiss Xradia Versa 520 X-ray computed tomography (CT) machine (160 kV, 10 W, 1 µm voxel size) was used to measure the pore structure. The X-ray CT allowed for a visual reconstruction and quantification of the pore structures. The ImageJ (FIJI) 3D Objects Counter was used to quantify the pore sizes and morphologies from the image stacks obtained by X-ray CT [44]. Currently, in AM processes, there are three main classifications of pores: gas pores, lack-of-fusion (LOF) pores, and keyhole pores [24]. The pores in this study were classified by aspect ratios, which is the ratio of the minor axis to the major axis of the best fitting ellipse of the pore. The pores were classified as either a gas pore (aspect ratio greater than 0.5) or a LOF pore (aspect ratio less than or equal to 0.5). There is a threshold of laser-energy density, which is typically higher than the optimal laser-energy density, above which an increase in keyhole porosity results [45,46]. In the current work, the laser-energy density for the three build conditions likely does not surpass this threshold, so no classification of keyhole porosity was performed. Additionally, an equivalent spherical diameter was determined by calculating the diameter of a sphere of equivalent volume of the pore. Finally, a relative, volumetric density of the specimen was calculated using the total volume of the CT scan and the total volume of the pores.

A specimen from each build condition was sectioned in three orthogonal directions (with respect to the loading direction), ground with SiC paper (400 grit through 1200 grit), polished with suspensions of 3  $\mu$ m and 1  $\mu$ m diamond particles, and finished with a vibratory polish using 50 nm colloidal silica. Backscattered electron (BSE) images were acquired using a field-emission scanning electron microscope (FE-SEM) at 20 kV, 60  $\mu$ m aperture, and a 7.8 mm working distance. Electron backscatter diffraction (EBSD) measurements were conducted in an FE-SEM (20 kV, 120  $\mu$ m aperture, 7.8 nA probe current, and 19.0 mm

working distance) using a 0.50  $\mu$ m step size. EBSD measurements were cleaned with standard practices in the TSL OIM Analysis software (v7) to remove points with a low confidence index (primarily occurring in the lack-of-fusion regions). Energy dispersive spectroscopy (EDS) line scans were carried out in an FE-SEM with a 1 nm step size and a 6 kV accelerating voltage to minimize interaction volume but maintain sufficient excitation energy. Following mechanical testing, fractography was performed using a thermionic emission SEM (20 kV and a 19 mm working distance) and a secondary electron (SE) detector.

# 3. Results

# 3.1. Characterization of as-received material

X-ray CT was used to quantify differences in porosity among the three build conditions. Visual reconstructions of the pore structure are shown in Fig. 2a-c. The reconstructions capture only the gas porosity (i.e., the small, spherical pores) and the LOF porosity (i.e., the large, non-spherical pores). The LOF pores were defined as those having an aspect ratio of less than 0.5, which indicates non-sphericity. The remaining pores, which were more spherical, were classified as gas pores. Quantifying both the gas porosity and the LOF porosity using equivalent spherical diameter allows for the relative frequency with respect to pore size to be compared in Fig. 2d. The specimen built at 0° orientation with a 38 J/mm<sup>3</sup> laser-energy density contained significantly more porosity than the other two build conditions. This porosity was dominated by LOF pores. Additionally, the specimen built at 0° orientation with a 62 J/mm<sup>3</sup> laser-energy density had more LOF porosity than the specimen built at 60° orientation with the same laser-energy density (62 J/mm<sup>3</sup>). As shown in the pore-frequency plot in Fig. 2d, all three build conditions exhibited similar frequency of pore sizes for pores classified as gas porosity. In all three build conditions, the spherical gas porosity constitutes less than 0.3% of the entire sample volume (Table 2). Additionally, the LOF porosity for the first build condition (0° and 38 J/mm<sup>3</sup>) comprises a small number of very large sized pores (greater than 75 µm in diameter). Although the X-ray CT visual reconstructions of porosity show a large amount of porosity, the two build conditions manufactured with the high laser-energy density (62 J/ mm<sup>3</sup>), but with different build orientations (0° and 60°), have a high relative part density: 99.77% and 99.93%, respectively. In contrast, the relative part density of the build condition manufactured with the low laser-energy density (38 J/mm<sup>3</sup>) was 93.09%, where LOF porosity

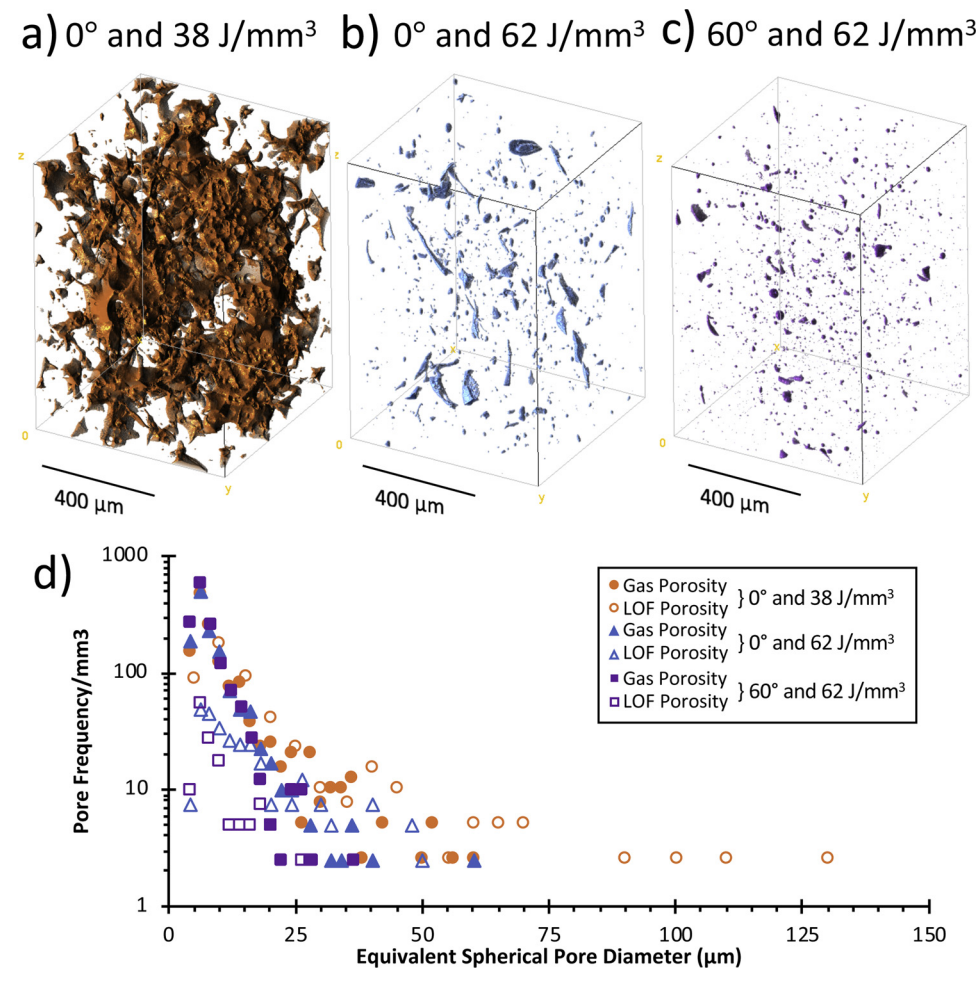


Fig. 2. X-ray CT reconstruction of porosity (the tensile direction is vertical) for the following build conditions: (a)  $0^{\circ}$  build orientation and  $38 \text{ J/mm}^3$  laser-energy density, (b)  $0^{\circ}$  build orientation and  $62 \text{ J/mm}^3$  laser-energy density, and (c)  $60^{\circ}$  build orientation and  $62 \text{ J/mm}^3$  laser-energy density. (d) Frequency of porosity by equivalent spherical pore diameter per build condition showing both gas porosity and lack-of-fusion porosity.

**Table 2**Porosity values (% by volume for a given part) for each build condition showing the relative density, the gas porosity, and the lack-of-fusion porosity.

Build condition	Build orientation (°)	Laser- energy density (J/mm <sup>3</sup> )	Relative density (%)	Gas porosity (%)	Lack-of- fusion porosity (%)
1	0	38	93.09	0.29	6.62
2	0	62	99.77	0.11	0.12
3	60	62	99.93	0.06	0.01

comprises a majority of the porosity (6.62%).

EBSD was used to quantify differences in effective grain sizes, grain morphologies, and crystal orientations among the three build conditions. To achieve this, a large area EBSD map was acquired in three orthogonal planes (with respect to tensile direction) for each build condition. The inverse pole figure (IPF) maps (Fig. 3) were carefully analyzed so that each orthogonal view shows poles (plane normals in a given grain) rotated in reference to a common direction (the build direction). Fig. 3a, b, and i show both the direction of hatch filling and the width of the laser passes from the manufacturing process (see dashed arrows in 3 b). In the  $0^\circ$  and  $38\,\mathrm{J/mm^3}$  build condition, EBSD measurements revealed smaller grain structures compared to the  $0^\circ$  and  $62\,\mathrm{J/mm^3}$  build condition. Additionally, the hatching is more pronounced in the high laser-energy density  $(62\,\mathrm{J/mm^3})$  build condition (Fig. 3b) compared to the low laser-energy density  $(38\,\mathrm{J/mm^3})$  build

condition (Fig. 3a). Fig. 3c, g, and h show the melt-pool geometry and microstructure perpendicular to the build direction for all build conditions. In general, a characteristic feature observed in the microstructure for all three build conditions was the grain morphology. Specifically, most grains appeared elongated in a trajectory parallel to the build direction. In the analysis software, texture maps (intensities displayed on inverse pole figures) were computed using a harmonic series expansion and a triclinic sample symmetry (no sample symmetry), as opposed to an orthotropic sample symmetry (like a rolled sheet), so as to not compute erroneous symmetry assumptions. All three build conditions exhibited a similar texture (i.e., the <001> pole orientations were aligned with the build direction), which is shown in Fig. 4. However, the maximum intensity of the 0° and 38 J/mm<sup>3</sup> build condition (1.61) was less than the maximum intensities of the other two build conditions (2.01 for the 0° and 62 J/mm<sup>3</sup> build condition and 2.35 for the 60° and 62 J/mm<sup>3</sup> build condition).

Large black regions shown in Fig. 3a, d and g are areas with a near-zero confidence index and correspond directly with the location of both gas pores and LOF pores (large LOF pores are most prevalent in the  $0^\circ$  and  $38\,\mathrm{J/mm^3}$  build condition). The LOF pores were observed in the other two build conditions as well, but to a lesser extent in terms of both size and frequency. A characteristic feature observed around most LOF pores was the presence of small grains. The  $0^\circ$  and  $38\,\mathrm{J/mm^3}$  build condition exhibited the smallest effective grain size (width of grains in the direction of tension) of the three build conditions; whereas, the  $60^\circ$  and  $62\,\mathrm{J/mm^3}$  build condition had the largest.

In addition to the grain morphology, which was elongated in the

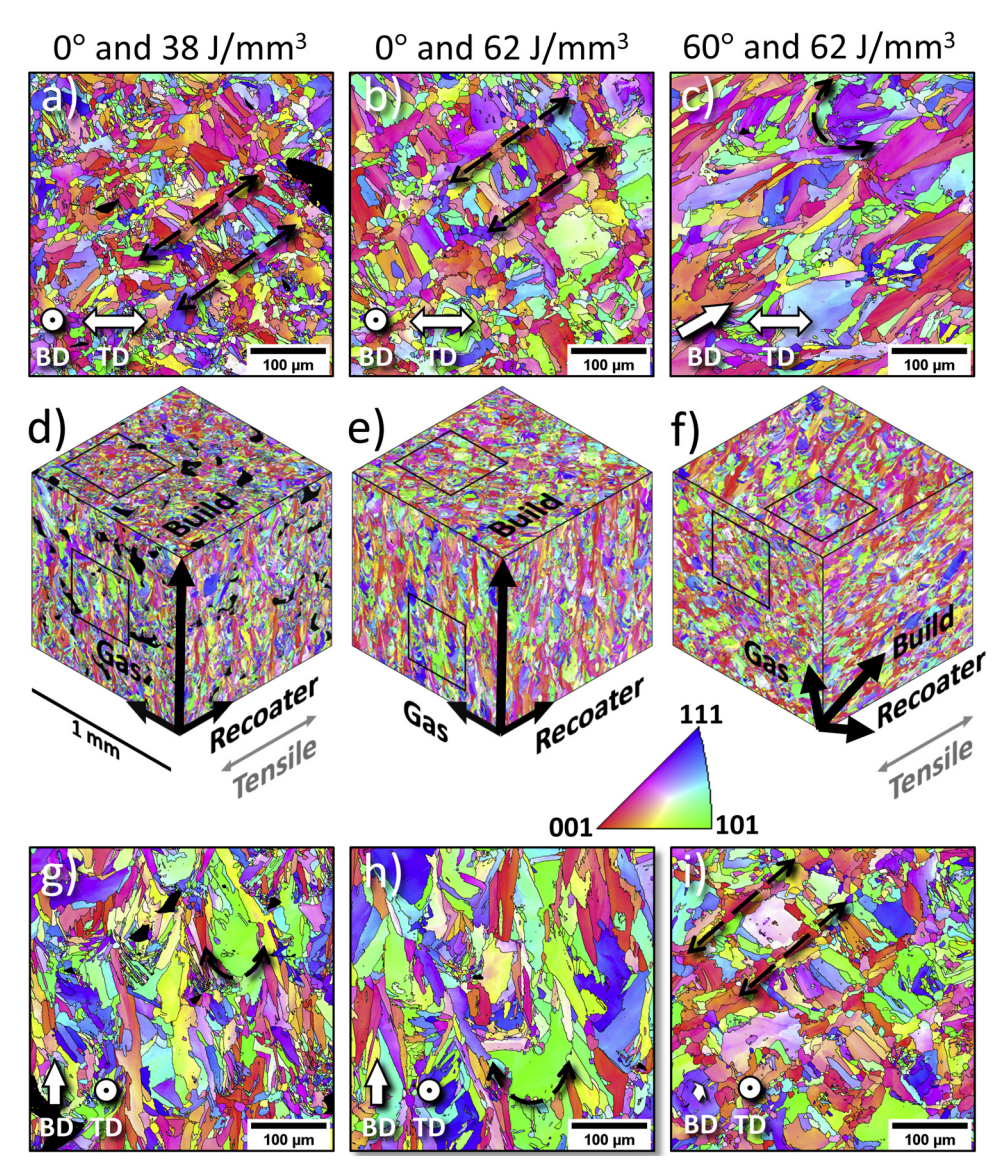


Fig. 3. EBSD reconstruction of inverse pole figure maps for planes parallel and normal to the tensile direction (TD) for three different build conditions: (a,g) 0° and  $38 \text{ J/mm}^3$ ; (b,h) 0° and  $62 \text{ J/mm}^3$ ; and (c,i) 60° and  $62 \text{ J/mm}^3$ , where BD stands for build direction. Inverse pole figure maps for all three orthogonal planes shown with respect to gas flow, recoater, build, and tensile directions: (d) 0° and  $38 \text{ J/mm}^3$ , (e) 0° and  $62 \text{ J/mm}^3$ , (f) 60° and  $62 \text{ J/mm}^3$ . All inverse pole figure maps are plotted with respect to the BD.

build direction, the L-PBF IN718 microstructure contained a sub-grain structure with apparent growth directions parallel to the building direction (see arrows in Fig. 5a) and appeared as columnar sub-grains. The sub-grain growth appears cellular in nature (Fig. 5b) when viewed in a direction parallel to the build direction. The columnar and cellular sub-grain structure are the same structure viewed in different orientations (i.e., a cylindrical structure in three dimensions). The spacing of

the sub-grain structure was measured using a method where the number of sub-grain structures was counted per 5 or  $10\,\mu m$  line segments. The number of sub-grains per  $\mu m$  was then converted to a spacing value representing the average spacing between sub-grain structures and compared among the three build conditions. The first, second, and third build conditions showed an average spacing of 0.34, 0.69, and 0.5  $\mu m$ , respectively. Additionally, the BSE images clearly highlight a

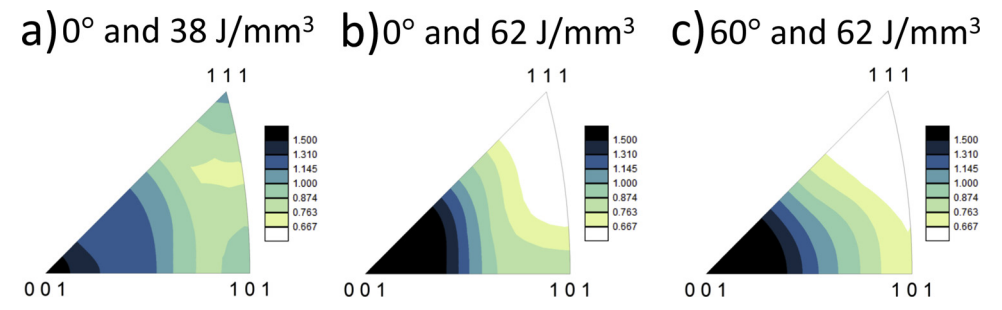


Fig. 4. The texture heatmaps (harmonic series expansion of grain orientations) for the three different build conditions.

Fig. 5. BSE images showing the sub-grain structures with apparent growth parallel to the build direction for (a) the  $0^{\circ}$  and  $38 \,\mathrm{J/mm^3}$  build condition, (b) the  $0^{\circ}$  and  $62 \,\mathrm{J/mm^3}$  build condition, and (c) the  $60^{\circ}$  and  $62 \,\mathrm{J/mm^3}$  build condition.

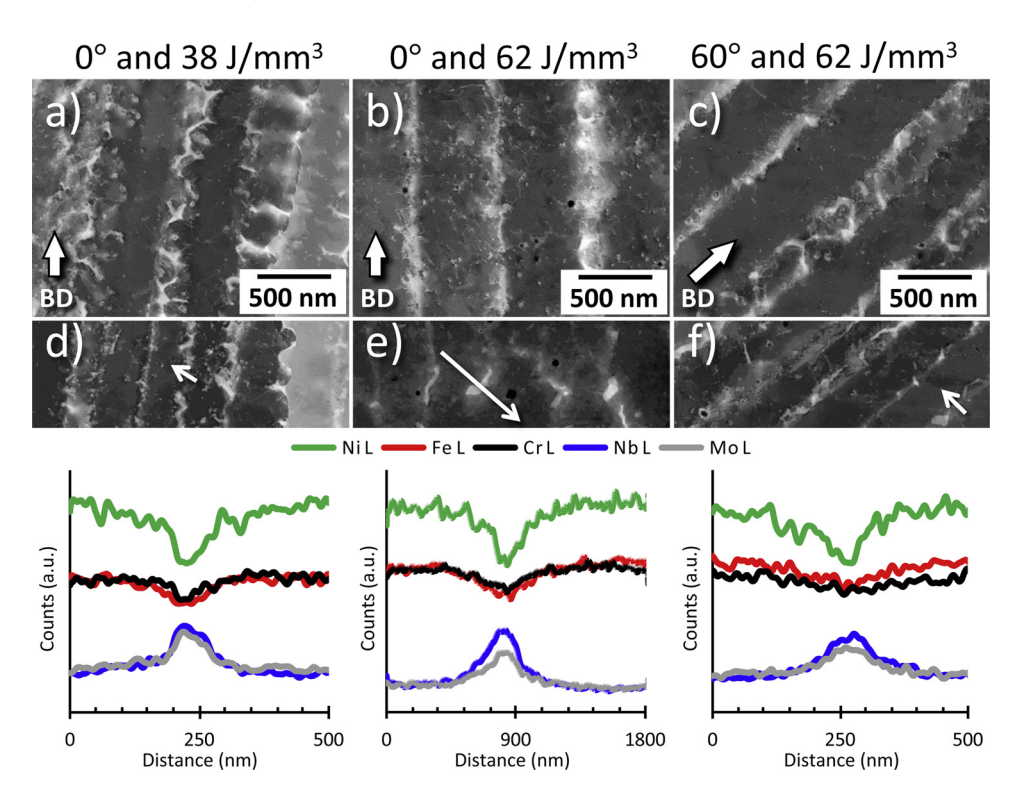


Fig. 6. BSE images showing the precipitates located on the cellular dislocation structures: (a) first build condition (0° and  $38 \text{ J/mm}^3$ ), (b) second build condition (0° and  $62 \text{ J/mm}^3$ ), and third build condition (60° and  $62 \text{ J/mm}^3$ ). EDS line scans (elemental counts from L- $\alpha$  lines) of Ni, Fe, Cr, Nb, and Mo, along the direction of the white arrow shown in (d), (e), and (f) for the three build conditions, respectively.

distinct melt-pool boundary, shown in Fig. 5c. Growth of the sub-grains from the melt-pool boundary is well distinguished. Fig. 6d provides a high magnification view of the sub-grain structure and reveals cells/walls of dislocations, which are decorated with secondary nano-scale precipitates. To determine the elemental composition of those precipitates, EDS line scans were performed at high magnification. Fig. 6a shows a BSE image from which a line scan was acquired, and Fig. 6b shows the X-ray intensity corresponding to Fe, Nb, Cr, Mo, and Ni. The secondary precipitates are enriched in Nb and Mo and depleted in Ni, Cr, and Fe. No differences in particle morphologies were observed among the three as-built conditions.

#### 3.2. Tensile properties

All measured engineering stress-strain curves are shown in Fig. 7a–c for the three build conditions. The first build condition (0° and 38 J/mm³) exhibited the lowest tensile strength and lowest elongation. This build condition had an average yield strength (YS) of 639 MPa  $\pm$  10 MPa, which is approximately 18% lower than the other build conditions. Additionally, the ultimate tensile strength (UTS) of this build condition (774 MPa  $\pm$  22 MPa) was approximately 28% lower than the other two build conditions (1081 MPa  $\pm$  23 MPa and 1070 MPa  $\pm$ 

34 MPa, respectively). The Young's modulus of the second and third build conditions (0° and 60° oriented parts manufactured with a laserenergy density of 62 J/mm<sup>3</sup>) was approximately 195 GPa; whereas, the Young's modulus for the 0° and 38 J/mm<sup>3</sup> build condition was 150 GPa ± 22 MPa. A summary of the YS, UTS, uniform elongation (UE), and total elongation (TE) is shown in Fig. 7d and e. The average UE (0.05  $\pm$  0.007) and TE (0.06  $\pm$  0.012) of the 0° and 38 J/mm<sup>3</sup> build orientation were approximately 77% lower than the UE  $(0.22 \pm 0.013 \text{ and } 0.21 \pm 0.034)$  and TE  $(0.29 \pm 0.027 \text{ and }$  $0.28 \pm 0.085$ ) of the second and third build conditions. No significant difference was found when comparing the UTS, UE, and TE of the 0° and 62 J/mm<sup>3</sup> and the 60° and 62 J/mm<sup>3</sup> build conditions, but a significant difference in YS was measured between the two. Finally, the YS, UTS, and Young's modulus for the second and third build conditions are comparable to that of wrought IN718 (Table 3). The ANOVA results showed that between the first build condition (0° and 38 J/mm<sup>3</sup>) and the second build condition (0° and 62 J/mm<sup>3</sup>), there were statistically significant differences in YS, UTS, Young's modulus, UE, and TE (all p < 0.001). The ANOVA between the first build condition and third build condition (60° and 62 J/mm<sup>3</sup>) showed similar differences observed between the first and second build conditions. Additionally, the comparison between the second and third build conditions showed only

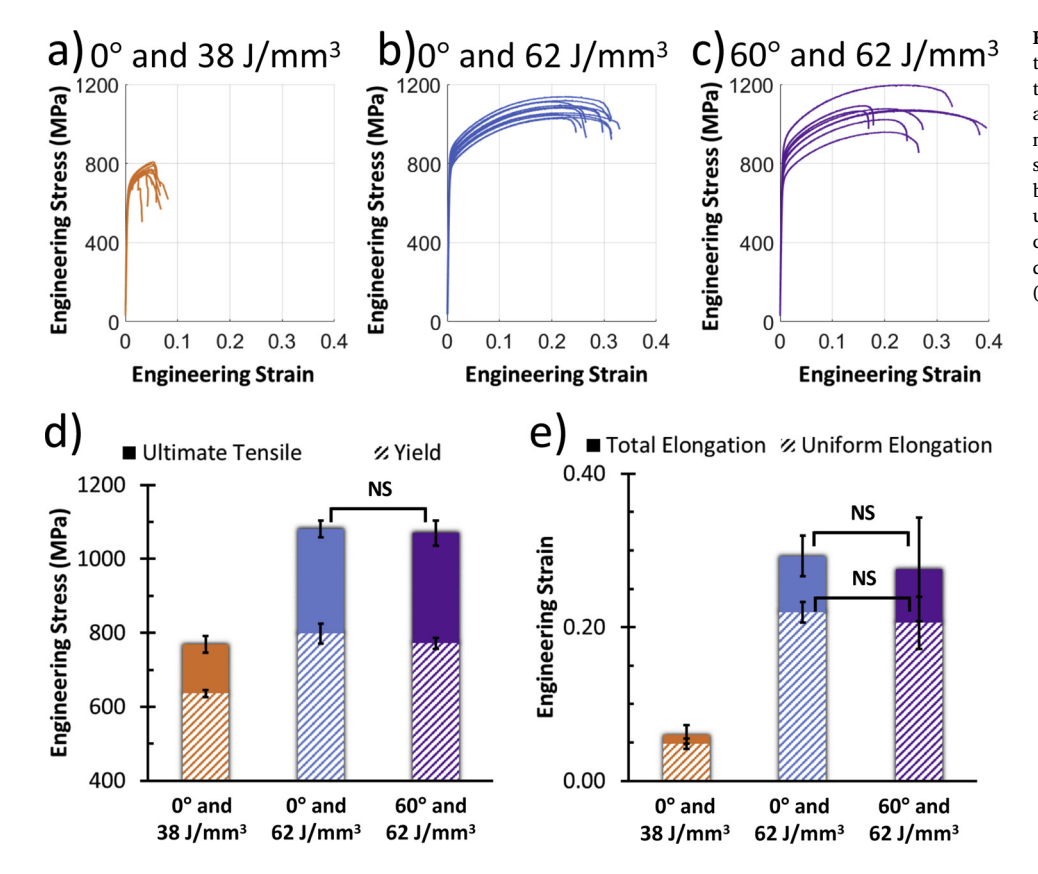


**Fig. 7.** Engineering stress-strain curves for (a) the first build condition (0° and  $38 \text{ J/mm}^3$ ), (b) the second build condition (0° and  $62 \text{ J/mm}^3$ ), and (c) the third build condition (60° and  $62 \text{ J/mm}^3$ ). (d) Summary of the average yield strength and ultimate strength for the three build conditions. (e) Summary of the average uniform and total elongation for the three build conditions. Error bars indicate one standard deviation and NS stands for not significant (p < 0.05).

a statistically significant difference in YS (p < 0.05).

## 3.3. Fractography

The fracture surfaces from the 0° and 38 J/mm³ build condition contained undulating features (Fig. 8a) due to a high amount of porosity, which is consistent with the high amount of porosity observed in the X-ray CT measurements. Only small pores are visible on the fracture surfaces of the build conditions manufactured with a high laser-energy density (Fig. 8b and c). The fracture surfaces of all three build conditions have regions of ductile micro-void coalescence (Fig. 8d) and signs of brittle failure near LOF pores (Fig. 8e). Sub-grain structures visible in BSE images of the microstructure were also observed in the fracture surfaces (Fig. 8f).

## 4. Discussion

## 4.1. Effects of laser-energy density

In the first two build conditions, build orientation was the same  $(0^{\circ})$ , but the L-PBF beam settings varied to study the effects of laser-energy density (38 and 62 J/mm<sup>3</sup>) on the three-dimensional pore structure and microstructure. One effect from using the low laser-energy density (38 J/mm<sup>3</sup>) in L-PBF is the formation of a large amount of LOF pores.

Results from X-ray CT in Section 3.1 show that the specimens manufactured with the low laser-energy density (38 J/mm<sup>3</sup>) contained the higher amount of porosity (6.91% of the analyzed volume) compared to the 62 J/mm<sup>3</sup> laser-energy density porosity (0.23% of the analyze volume). Using optical microscopy, Moussaoui et al. [26] showed that the porosity for L-PBF IN718 was approximately 0.8% and 0.48% for 40 and 61.2 J/mm<sup>3</sup> laser-energy densities, respectively, indicating that for this range of laser-energy density the porosity content decreases as laser-energy density increases (once the laser-energy density is high enough to start forming keyhole pores, the porosity will begin to increase). Fairly similar amounts of porosity were observed for the current work and work from Moussaoui et al. [26] for the laser-energy density near 62 J/mm<sup>3</sup>. However, the low laser energy density (i.e., near 38 J/mm<sup>3</sup>) showed large differences in porosity (6.91% compared to 0.8%). Although Moussaoui et al. showed different amounts of porosity for the two laser-energy densities, they performed a two-dimensional analysis of the pore structure using optical microscopy (the current study used X-ray CT). Therefore, a direct comparison between the two-dimensional analysis by Moussaoui et al. [26] and the threedimensional analysis in this work was difficult. It is likely that the 38 J/ mm<sup>3</sup> laser-energy density represents a lower bound on sufficient laserenergy density in terms of proper melting parameters. In this work, most of the porosity in the low laser-energy density build condition was characterized as LOF pores, which are formed due to an insufficient

Table 3

The average yield strength, ultimate tensile strength, Young's modulus, uniform elongation, and total elongation of all three build conditions for L-PBF IN718 (with one standard deviation). References are provided for the wrought condition.

Build condition	Build orientation	Laser-energy density J/mm <sup>3</sup>	Yield strength MPa	UTS MPa	Young's modulus GPa	Uniform elongation	Total elongation
1	0	38	639 (10)	774 (22)	151 (22)	0.05 (0.007)	0.06 (0.012)
2	0	62	798 (27)	1081 (23)	195 (17)	0.22 (0.013)	0.29 (0.027)
3	60	62	772 (15)	1070 (34)	194 (26)	0.21 (0.034)	0.28 (0.085)
n/a	W	rought	800–1100 [25,47]	1200–1400 [48]	208 [48]	n/a	0.32 [49]

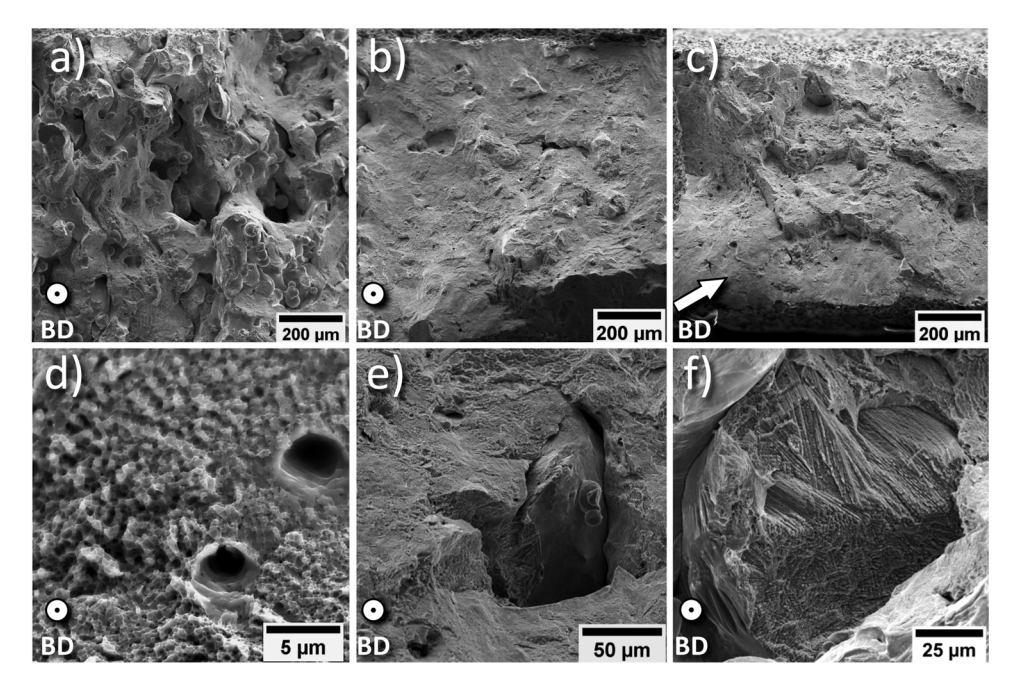


**Fig. 8.** Representative SEM images of the fracture surfaces for the following build conditions: (a) 0° and 38 J/mm³, (b) 0° and 62 J/mm³, and (c) 60° and 62 J/mm³. A representative SEM image of (d) micro-void coalescence and gas porosity, (e) cleavage-like fracture near LOF porosity, and (f) the sub-grain structure observed on the fracture surfaces in the rupture zone of the 0° and 62 J/mm³ build condition.

melting of the powder particles [19,50]. Small and spherical pores were also observed in all build conditions, which may originate from hollow powder particles or keyhole collapse [51]. Even though a similar distribution of spherical pore sizes was observed in all build conditions, the 0° and 38 J/mm³ build condition contained nearly twice the amount of spherical gas pores as the other two build conditions (Table 2). The gas pores are typically attributed to the powder characteristics, which should remain constant throughout the different build conditions in this work. However, due to the rough classification method used (i.e., aspect ratio), some LOF pores likely were misclassified as gas pores [52], causing differences in the represented gas porosity values.

The laser-energy density also influenced many aspects of the grain and sub-grain structure. The 38 J/mm<sup>3</sup> laser-energy density specimen contained the smallest effective grain sizes due to two mechanisms. First, around the LOF pores, a grain refinement was observed, which is consistent with observations by Pei et al. [53] of clustered fine-grain zones around pores. Pei et al. [53] concluded that the pores stopped the grain growth due to disrupting the temperature gradient along the build direction. Second, the melt-pool geometries visible in the microstructure (Fig. 3) were smaller for the 38 J/mm<sup>3</sup> laser-energy density (compared to the 62 J/mm<sup>3</sup> laser-energy density). Generally, a lower laser-energy density produces less energy input, ultimately reducing the size of the melt-pool [54]. Furthermore, on the plane normal to the build direction, the scan tracks can be observed (Fig. 3a and b). In both laser-energy densities, the width of the tracks is approximately 100 µm, which can be expected since hatch spacing for both parts was the same (100 μm). However, the scan tracks observed in the 38 J/mm<sup>3</sup> laserenergy density appeared to have a much more irregular pattern (Fig. 3a) indicative of a high melt-pool instability, which shows a high fluctuation in melt-pool dynamics [55]. A strong texture was observed for both laser-energy densities, such that the majority of <001>-oriented grains aligned with the build direction.

Sub-grain structures were observed for both the 38 and  $62 \,\mathrm{J/mm^3}$  energy densities. There was an average spacing of  $0.34\,\mu\mathrm{m}$  in the  $38 \,\mathrm{J/mm^3}$  laser-energy density specimens compared to  $0.69\,\mu\mathrm{m}$  in the  $62 \,\mathrm{J/mm^3}$  laser-energy density specimens. The sub-grain structure consists of dislocation sub-structures that form when large amounts of low-energy dislocations cluster [56] to form geometric boundaries that are necessary to accommodate plastic strain [57] exerted by the manufacturing process. Tucho et al. [58] showed that the number of the clustered dislocations is indicative of the amount of plastic deformation created

by extreme thermal histories (rapid solidification) in AM processes, meaning a higher number of sub-grain structures, which correlates to a smaller sub-grain spacing, indicates a greater amount of residual stress produced during the manufacturing process. Bertoli et al. [59] showed that lower values of laser power at the same scan speeds (i.e., lower laser-energy densities) had higher cooling rates in L-PBF titanium. The low laser-energy density (38 J/mm³) specimens in this work showed the smallest spacing, which indicates a higher number of sub-grains, likely experienced higher cooling rates and a higher amount of residual stress as compared to the 62 J/mm³ laser-energy density specimens.

Although the sub-grain spacing was different between the two laser energy densities, the precipitates that decorated the sub-grain structures were similar in both morphology and composition. Microsegregation of Nb to sub-grain boundaries has been reported for AM IN718 [38,60] and IN718 Plus [61]. MC type carbides are rich in Nb and Mo [62,63] and are commonly found in Inconel alloys near irregularly shaped Laves phase particles [64,65]. While the  $\delta$  phase is also enriched in Nb and Mo, the  $\delta$  phase is always characterized by a needle-like morphology [32]. Since none of the observed precipitates had a needle-like morphology (whether on sub-grain boundaries or grain boundaries), it is likely that the precipitates observed in all three as-built conditions are Laves phase mixed with MC type carbides, which was shown to be prevalent in L-PBF IN718 [58,66,67].

The difference in laser-energy density produced statistically significant differences in all measured tensile properties (Fig. 7 and Table 3), most likely due to the large amount of LOF pores and differences in thermal history. A comparison between fracture surfaces of specimens produced with different laser-energy densities (Fig. 8a and b) shows the vast difference in the amount of LOF that contributed to premature failure and a loss of ductility in the low laser-energy density condition. Since the cross-sectional area was measured on the outside of the specimen, the engineering stress was likely underestimated since the 6.91% (volumetric) internal porosity was not accounted for, but this volume-averaged value does not completely account for the nearly 20% difference in strength when comparing the same build orientation. It is likely that the worst case cross-sectional area of porosity (11% in a twodimensional slice), coupled with the smaller grain size and higher subgrain density, could account for the differences in tensile properties. However, it is not possible to decouple the effects of the porosity, grain size, and sub-grain density on the mechanical properties due to the dominating effects from the large and numerous LOF pores.

Additive Manufacturing 36 (2020) 101425

#### 4.2. Effects of build orientation given the same laser-energy density

The second and third build conditions have the same laser-energy density (62 J/mm<sup>3</sup>) and vary the build orientation: 0° and 60°, respectively. The X-ray CT results showed that the 0° build condition contained 0.23% porosity (by volume), but only 0.07% porosity (by volume) in the 60° build condition was gas porosity (Table 2). Although these two build conditions were manufactured with the same laserenergy density, the laser powers and scan speeds were different (Table 1). The build condition at 0° orientation had a faster scan speed (1770 mm/s) than the 60° orientation (1180 mm/s). Aboulkhair et al. [68] showed that in L-PBF aluminum, faster laser scan speeds produce more LOF pores. In the current work, there is an increase in laser scan speed and laser power equalling the same laser-energy density. Kamath et al. [21] showed that an increase in laser scan speed had a larger influence on the porosity than laser power because the higher laser scan speed did not provide a sufficient amount of penetrating energy into the powder-bed system to completely melt the powder. This insufficient energy penetration led to a higher amount of porosity. Therefore, the difference in LOF porosity between the two build conditions at the same laser-energy density can be attributed to the different laser scan speeds.

When comparing effective grain sizes of the second and third build conditions (0° and 60°), the third build condition had a larger effective grain size based on line-intercept measurements along the loading direction. Visualizing the gas-recoater and build-recoater planes (see Fig. 3e and Fig. 3f) provides insight to explain the slight differences in effective grain size with respect to the loading direction. The average grain widths, measured over a 1 mm × 1 mm area in the gas-recoater plane using a line-intercept method along the loading direction, are 9.4 and  $13.2\,\mu m$  for the  $0^\circ$  and  $60^\circ$  build orientations, respectively. Higher magnification views are shown in Fig. 3b and c. As shown in this work and previous work (e.g., [25,29,30,34]), the grains in as-built AM microstructures are elongated in the build direction. The specimens built at 60° had grains slightly elongated towards the build direction, causing larger effective grains measured with respect to the loading direction. The crystallographic texture for both of these build conditions was similar, and further analysis of the Schmid factors in each build orientation (with respect to tensile direction) indicated that the averages were approximately the same, indicating that effective grain size was the main difference in microstructure. Differences of sub-grain spacing existed for the two different build orientations (0° and 60°) at the same laser-energy density (62 J/mm<sup>3</sup>). The average sub-grain spacing was 0.69 and  $0.50\,\mu m$  for the  $0^\circ$  and  $60^\circ$  specimens, respectively. As previously shown [58], a smaller sub-grain spacing indicates a greater amount of residual stress induced by the manufacturing process. Therefore, this difference in sub-grain spacing indicates that the amount of residual stress due to the manufacturing process in the 60° specimens was slightly greater than that in the 0° specimens. Deng et al. [69] attributed differences in the amount of residual stress in specimens built at the same laser-energy density to differences in the build orientation of specimens. In the current work, the 60° specimens had less overlap and remelting of previous layers due to the orientation in which they were built. There has also been evidence in the literature showing that the remelting of previous layers can lead to a reduction in accumulated strains, effectively acting as a stress relieving process [70–72]. Therefore, it can be postulated that the increased remelting of previous layers in the 0° specimens decreased the amount of residual stress (compared to the 60° specimens) and ultimately led to a larger subgrain spacing. Additionally, the precipitates that decorate the sub-grain structures were similar in both morphology and composition for the two build orientations (0° and 60°).

The effects of build orientation on the tensile properties were less drastic than the effects from using a non-optimized laser-energy density. The ANOVA between the two build conditions produced no statistically significant difference in the UTS, UE, TE, and Young's modulus. The minor differences in porosity (attributed to the change in scan

speed) did not have a statistically significant effect on the tensile properties. However, there was a statistically significant difference between the yield strengths of the two build orientations but same laser-energy density. The 60° build orientation exhibited a slightly lower yield strength than the 0° build orientation. The smaller effective grain sizes in the 0° build orientation, with respect to the loading direction, would lead to a shorter dislocation mean free path and thus a higher yield strength according to the Hall-Petch effect [73]. Additionally, the standard deviations for the tensile properties were much larger for the 60° build orientation compared to the 0° build orientation. In the 60° build orientation specimens, there was a variation in build height (i.e., specimens taken from the bottom and top grip region): whereas, the specimens from the 0° build orientation were taken from nominally the same build height. Previous research has shown that build height has an effect, albeit sometimes small, on the mechanical properties in L-PBF metals [74–77] due to variations in grain structures.

## 4.3. Relationship to previous work on high-cycle fatigue life

The previous fatigue work by the authors [39] investigated the relationships between AM build conditions, surface roughness, and high-cycle fatigue life for as-built L-PBF IN718. However, no pre-mortem investigation into the material structures was performed. To better understand the full processing-structure-property relationships for as-built L-PBF IN718, this work focused on investigating the micro-structure (grain and sub-grain structures) and internal porosity. The relationships among the laser-energy density, build orientation, three-dimensional pore structure, grain structure, sub-grain structure, and quasi-static tensile properties were studied. As previously mentioned, this work used three build conditions that resulted in the extreme cases of fatigue life, while exhibiting variability in the laser-energy density and build orientation.

From the previous work [39], the differences in laser-energy density at the same build orientation showed a large difference in high-cycle fatigue life (10,755 cycles and 60,919 cycles, on average, for the 38 and 62 J/mm3 laser-energy densities, respectively, and 0° build orientation). The fatigue work showed that there was no significant difference between surface roughness values, for the aforementioned build conditions, so the difference in fatigue life was mainly attributed to internal porosity differences, which was supported by fractographic analysis of the fatigue failure surfaces. The current work quantified, comprehensively and in three dimensions, the difference in porosity and showed that the porosity had a large effect on the quasi-static tensile properties. The 38 J/mm<sup>3</sup> laser-energy density specimen exhibited roughly 6.91% porosity while also having the lowest quasi-static tensile properties; the findings confirm that the porosity plays a key role in the fatigue life. However, other factors were likely to have influenced the observed differences in fatigue life. Fatigue life can be sensitive to residual stresses, and the current work demonstrates that the differences in subgrain spacing could indicate a difference in the residual stress caused by differences in the laser processing parameters (i.e., the laser-energy density). In other words, although the internal porosity dominates the observed differences in fatigue life, given the same surface roughness, the differences in residual stress likely had an influence as well. Additionally, when comparing the different build orientations (0° and 60° at 62 J/mm<sup>3</sup> laser-energy density), the previous work showed a significant difference in high-cycle fatigue life (60,919 cycles and 172,497 cycles, on average, respectively). Results from the fatigue study showed that the difference in fatigue life for the aforementioned build condition was primarily driven by the differences in the surface roughness and identified no differences in porosity. However, the current work showed slight differences in porosity between the two different build orientations. The only significant difference in quasi-static tensile properties between the different build orientations, given the same laser-energy density, was the yield strength. Therefore, the differences in porosity (0.23% and 0.07%, respectively) generally did not influence

the quasi-static properties but may have still had an influence on the high-cycle fatigue life since fatigue life has been shown to be sensitive to small changes in porosity, specifically in AM metals [78–80,23]. Similarly to the observed difference in the sub-grain structure between the different laser-energy densities (but same build orientation), there was also a difference in sub-grain spacing between the two build orientations with a fixed laser-energy density. This indicates a difference in residual stresses causes a difference in the high-cycle fatigue life. The first build condition consisted of the smallest spacing of sub-grain structures resulting from the highest amount of residual stress. The first build condition also correlates with the lowest high-cycle fatigue life among the three build conditions.

#### 5. Conclusions

In this study, the influence of the build orientation and laser-energy density on the three-dimensional pore structure, microstructure, and the corresponding quasi-static tensile properties was investigated for asbuilt L-PBF IN718. Based on the experimental results, the following conclusions are made:

- 1. The variation of the three-dimensional pore structure was predominantly controlled by the laser-energy density. At the low laser-energy density (38 J/mm³), the applied energy was insufficient to fully melt the powder, which led to an increase in lack-of-fusion pores compared to the 62 J/mm³ laser-energy density. The first build condition (0° and 38 J/mm³) had a 93.09% relative density (6.91% porosity by total volume) compared to 99.77% for the 0° and 62 J/mm³ build condition. The relative volumetric density for the 60° and 62 J/mm³ build condition was 99.93%.
- 2. The grain structure was influenced by both the laser-energy density and the build orientation. The effective grain size was smaller in the 38 J/mm³ build condition compared to the 62 J/mm³. This was due to an observed grain refinement around the lack-of-fusion pores as well as a smaller melt pool geometry. A similar texture was observed for both the 38 and 62 J/mm³ laser-energy densities (both manufactured at a 0° build orientation). The effective grain sizes, based on a line intercept method used to measure the average grain width in the loading direction, were different between the two build orientations (manufactured with the same laser-energy density) since grains were elongated in the build direction causing a statistically significant difference in the yield strength.
- 3. Sub-grain structures were observed in the three build conditions that consist of dislocation sub-structures formed when large amounts of low-energy dislocations clustered to form geometric boundaries. A decrease in the spacing of these sub-grains can indicate a higher amount of residual stress caused by higher cooling rates during the manufacturing process. The first build condition (0° and 38 J/mm³) contained the smallest sub-grain spacing (0.34 µm) and the second build condition (0° and 62 J/mm³) contained the largest sub-grain spacing (0.69 µm). From the sub-grain spacing, the first build condition likely contains the highest amount of residual stress caused by the L-PBF process, and the second build condition contained the lowest amount.
- 4. The significant reduction in the yield strength and ultimate tensile strength for the 38 J/mm³ build condition, as compared to the 62 J/mm³ build condition, was attributed to the lack-of-fusion porosity. Although the microstructure differences have an effect on the mechanical properties, the individual effects cannot be decoupled due to the dominant influence of the porosity on the properties. The only significant difference in mechanical properties between the 0°- and 60°-oriented specimens was in the yield strength. The effective grain size in the 60° build specimens was slightly larger than in the 0° build specimens, which decreased the yield strength due to the longer mean free path for dislocation motion.
- 5. In all three build conditions, precipitates were observed at the end

- of the dislocation walls that are referred to as the sub-grain structures. These precipitates had a high amount of Nb and Mo, which are consistent with MC type carbides and Laves phase particles. Since all three build conditions were investigated in the as-built (non-heat-treated) condition, no other phases or precipitates were observed.
- 6. In L-PBF Inconel, the mechanical properties are influenced by the pore structure (which includes both gas porosity and lack-of-fusion porosity), and by the microstructure (which includes the grain size and morphology, the crystallographic texture, the sub-grain structure, and the precipitates/secondary phases). However, in unoptimized laser-energy density builds, the pore structure dominates the mechanical properties. Therefore, to best optimize the mechanical properties for L-PBF IN718, it is recommended to minimize the porosity through laser-energy density control.

#### Authors' contribution

Dillon S. Watring: conceptualization, methodology, experimentation, analysis, visualization, writing – original draft, writing – review and editing. Jake T. Benzing: conceptualization, methodology, experimentation, analysis, writing – review and editing. Nik Hrabe: conceptualization, methodology, resources, supervision, writing – review and editing. Ashley D. Spear: resources, supervision, writing – review and editing.

#### Conflict of interest

None declared.

## Acknowledgements

This research is supported by the Department of Defense Office of Economic Adjustment (ST1605-19-03) and by the National Science Foundation CAREER award (CMMI 1752400). The authors would like to express gratitude to 3D Systems for supplying the materials, National Institute of Standards and Technology (NIST) for providing access to testing equipment (EBSD, SEM, CT, and tension testing), and Dr. Nadia Kouraytem for the valuable discussion about this work. This research was performed while Jake Benzing held a National Research Council Postdoctoral Research Associateship at the National Institute of Standards and Technology.

#### References

- L. González-Fernández, L. Del Campo, R. Pérez-Sáez, M. Tello, Normal spectral emittance of inconel 718 aeronautical alloy coated with yttria stabilized zirconia films, J. Alloys Compds. 513 (2012) 101–106.
- [2] J. Lambarri, J. Leunda, V.G. Navas, C. Soriano, C. Sanz, Microstructural and tensile characterization of inconel 718 laser coatings for aeronautic components, Opt. Lasers Eng. 51 (7) (2013) 813–821.
- [3] E. Ezugwu, Z. Wang, A. Machado, The machinability of nickel-based alloys: a review, J. Mater. Process. Technol. 86 (1–3) (1999) 1–16.
- [4] E. Akca, A. Gürsel, A review on superalloys and in718 nickel-based inconel superalloy, Period. Eng. Nat. Sci. 3 (1) (2015) 15–27.
- [5] R. Molins, G. Hochstetter, J. Chassaigne, E. Andrieu, Oxidation effects on the fatigue crack growth behaviour of alloy 718 at high temperature, Acta Mater. 45 (2) (1997) 663–674.
- [6] X. Wang, X. Gong, K. Chou, Review on powder-bed laser additive manufacturing of inconel 718 parts, Proc. Inst. Mech. Engrs. Part B J. Eng. Manuf. 231 (11) (2017) 1890–1903.
- [7] J.-P. Costes, Y. Guillet, G. Poulachon, M. Dessoly, Tool-life and wear mechanisms of CBN tools in machining of inconel 718, Int. J. Mach. Tools Manuf. 47 (7–8) (2007) 1081–1087.
- [8] T. Sugihara, T. Enomoto, High speed machining of inconel 718 focusing on tool surface topography of CBN tool, Proc. Manuf. 1 (2015) 675–682.
- [9] A.K. Parida, K. Maity, Comparison the machinability of inconel 718, inconel 625 and monel 400 in hot turning operation, Eng. Sci. Technol. Int. J. 21 (3) (2018) 364–370.
- [10] B. Izquierdo, S. Plaza, J. Sánchez, I. Pombo, N. Ortega, Numerical prediction of heat affected layer in the EDM of aeronautical alloys, Appl. Surf. Sci. 259 (2012) 780–790

- [11] J.-P. Kruth, M.-C. Leu, T. Nakagawa, Progress in additive manufacturing and rapid prototyping, Cirp Annals 47 (2) (1998) 525–540.
- [12] M. Rehnberg, S. Ponte, 3d Printing and Global Value Chains: How A New Technology May Restructure Global Production, Global Production Networks Centre, Singapore, Copenhagen Business School, 2016.
- [13] Y. Huang, M.C. Leu, J. Mazumder, A. Donmez, Additive manufacturing: current state, future potential, gaps and needs, and recommendations, J. Manuf. Sci. Eng. 137 (1) (2015) 014001.
- [14] M. Baumers, Economic Aspects of Additive Manufacturing: Benefits, Costs and Energy Consumption, Loughborough University, 2012 Ph.D. thesis.
- [15] W.E. King, A.T. Anderson, R. Ferencz, N. Hodge, C. Kamath, S.A. Khairallah, A.M. Rubenchik, Laser powder bed fusion additive manufacturing of metals; physics, computational, and materials challenges, Appl. Phys. Rev. 2 (4) (2015) 041304.
- [16] S.A. Khairallah, A.T. Anderson, A. Rubenchik, W.E. King, Laser powder-bed fusion additive manufacturing: physics of complex melt flow and formation mechanisms of pores, spatter, and denudation zones, Acta Mater. 108 (2016) 36–45.
- [17] W.E. Frazier, Metal additive manufacturing: a review, J. Mater. Eng. Perform. 23 (6) (2014) 1917–1928.
- [18] P. Karimi, E. Sadeghi, D. Deng, H. Gruber, J. Andersson, P. Nylén, Influence of build layout and orientation on microstructural characteristics of electron beam melted alloy 718, Int. J. Adv. Manuf. Technol. 99 (2018) 2903–2913.
- [19] M. Tang, P.C. Pistorius, J.L. Beuth, Prediction of lack-of-fusion porosity for powder bed fusion, Addit. Manuf. 14 (2017) 39–48.
- [20] G. Vastola, Q. Pei, Y.-W. Zhang, Predictive model for porosity in powder-bed fusion additive manufacturing at high beam energy regime, Addit. Manuf. 22 (2018) 817–822.
- [21] C. Kamath, B. El-dasher, G.F. Gallegos, W.E. King, A. Sisto, Density of additively-manufactured, 316L SS parts using laser powder-bed fusion at powers up to 400 W, Int. J. Adv. Manuf. Technol. 74 (1–4) (2014) 65–78.
- [22] F. Imani, A. Gaikwad, M. Montazeri, P. Rao, H. Yang, E. Reutzel, Process mapping and in-process monitoring of porosity in laser powder bed fusion using layerwise optical imaging, J. Manuf. Sci. Eng. 140 (10) (2018).
- [23] L. Sheridan, O.E. Scott-Emuakpor, T. George, J.E. Gockel, Relating porosity to fatigue failure in additively manufactured alloy 718, Mater. Sci. Eng. A 727 (2018) 170–176.
- [24] R. Snell, S. Tammas-Williams, L. Chechik, A. Lyle, E. Hernández-Nava, C. Boig, G. Panoutsos, I. Todd, Methods for rapid pore classification in metal additive manufacturing, JOM (2019) 1–9.
- [25] K. Amato, S. Gaytan, L. Murr, E. Martinez, P. Shindo, J. Hernandez, S. Collins, F. Medina, Microstructures and mechanical behavior of inconel 718 fabricated by selective laser melting, Acta Mater. 60 (5) (2012) 2229–2239.
- [26] K. Moussaoui, W. Rubio, M. Mousseigne, T. Sultan, F. Rezai, Effects of selective laser melting additive manufacturing parameters of inconel 718 on porosity, microstructure and mechanical properties, Mater. Sci. Eng. A 735 (2018) 182–190.
- [27] J. Benzing, N. Hrabe, T. Quinn, R. White, R. Rentz, M. Ahlfors, Hot isostatic pressing (hip) to achieve isotropic microstructure and retain as-built strength in an additive manufacturing titanium alloy (ti-6al-4v), Mater. Lett. 257 (2019) 126690.
- [28] Q. Jia, D. Gu, Selective laser melting additive manufacturing of inconel 718 superalloy parts: densification, microstructure and properties, J. Alloys Compds. 585 (2014) 713–721.
- [29] L.L. Parimi, G. Ravi, D. Clark, M.M. Attallah, Microstructural and texture development in direct laser fabricated in718, Mater. Charact. 89 (2014) 102–111.
- [30] X. Wang, J.A. Mu niz-Lerma, O. Sánchez-Mata, M.A. Shandiz, M. Brochu, Microstructure and mechanical properties of stainless steel 316l vertical struts manufactured by laser powder bed fusion process, Mater. Sci. Eng. A 736 (2018) 27–40.
- [31] Y. Zhong, Sub-Grain Structure in Additive Manufactured Stainless Steel 316L, Department of Materials and Environmental Chemistry, Stockholm University, 2017 Ph.D. thesis.
- [32] T.G. Gallmeyer, S. Moorthy, B.B. Kappes, M.J. Mills, B. Amin-Ahmadi, A.P. Stebner, Knowledge of process-structure-property relationships to engineer better heat treatments for laser powder bed fusion additive manufactured inconel 718, Addit. Manuf. 31 (2020) 100977.
- [33] Y. Mu, C. Wang, W. Zhou, L. Zhou, Effect of nb on  $\delta$  phase precipitation and the tensile properties in cast alloy in625, Metals 8 (2) (2018) 86.
- [34] A. Mostafa, I. Picazo Rubio, V. Brailovski, M. Jahazi, M. Medraj, Structure, texture and phases in 3d printed in718 alloy subjected to homogenization and hip treatments, Metals 7 (6) (2017) 196.
- [35] G.M. Reddy, C.S. Murthy, K.S. Rao, K.P. Rao, Improvement of mechanical properties of inconel 718 electron beam welds-influence of welding techniques and postweld heat treatment, Int. J. Adv. Manuf. Technol. 43 (7-8) (2009) 671–680.
- [36] J.J. Schirra, R.H. Caless, R.W. Hatala, The effect of laves phase on the mechanical properties of wrought and cast + hip inconel 718, Miner. Metals Mater. Soc. (2015) 375–388.
- [37] C. Radhakrishna, K.P. Rao, S. Srinivas, Laves phase in superalloy 718 weld metals, J. Mater. Sci. Lett. 14 (24) (1995) 1810–1812.
- [38] M. Pröbstle, S. Neumeier, J. Hopfenmüller, L.P. Freund, T. Niendorf, D. Schwarze, M. Gökena, Superior creep strength of a nickel-based superalloy produced by selective laser melting, Mater. Sci. Eng. A 674 (2016) 299–3078, https://doi.org/10. 1016/j.msea.2016.07.061.
- [39] D.S. Watring, K.C. Carter, D. Crouse, B. Raeymaekers, A.D. Spear, Mechanisms driving high-cycle fatigue life of as-built inconel 718 processed by laser powder bed fusion, Mater. Sci. Eng. A 761 (2019) 137993.
- [40] E466-07, Standard Practice for Conducting Force Controlled Constant Amplitude Axial Fatigue Tests of Metallic Materials, Standard, ASTM International, 2007.

- [41] J. Ciurana, L. Hernandez, J. Delgado, Energy density analysis on single tracks formed by selective laser melting with cocrmo powder material, Int. J. Adv. Manuf. Technol. 68 (5-8) (2013) 1103–1110.
- [42] E3076-18, Standard Practice for Determination of the Slope in the Linear Region of a Test, Standard, ASTM International, 2018.
- [43] E8-16a, Standard Test Methods for Tension Testing of Metallic Materials, Standard, ASTM International, 2016.
- [44] J. Schindelin, I. Arganda-Carreras, E. Frise, V. Kaynig, M. Longair, T. Pietzsch, S. Preibisch, C. Rueden, S. Saalfeld, B. Schmid, et al., Fiji: an open-source platform for biological-image analysis, Nat. Methods 9 (7) (2012) 676.
- [45] W.E. King, H.D. Barth, V.M. Castillo, G.F. Gallegos, J.W. Gibbs, D.E. Hahn, C. Kamath, A.M. Rubenchik, Observation of keyhole-mode laser melting in laser powder-bed fusion additive manufacturing, J. Mater. Process. Technol. 214 (12) (2014) 2915–2925.
- [46] N. Kouraytem, X. Li, R. Cunningham, C. Zhao, N. Parab, T. Sun, A.D. Rollett, A.D. Spear, W. Tan, Effect of laser-matter interaction on molten pool flow and keyhole dynamics, Phys. Rev. Appl. 11 (6) (2019) 064054.
- [47] T. Trosch, J. Str"oßner, R. Völkl, U. Glatzel, Microstructure and mechanical properties of selective laser melted inconel 718 compared to forging and casting, Mater. Lett. 164 (2016) 428–431.
- [48] Z. Wang, K. Guan, M. Gao, X. Li, X. Chen, X. Zeng, The microstructure and mechanical properties of deposited-in718 by selective laser melting, J. Alloys Compds. 513 (2012) 518–523.
- [49] Y.-T. Chen, A.-C. Yeh, M.-Y. Li, S.-M. Kuo, Effects of processing routes on room temperature tensile strength and elongation for inconel 718, Mater. Des. 119 (2017) 235–243.
- [50] H. Gong, K. Rafi, H. Gu, T. Starr, B. Stucker, Analysis of defect generation in ti-6al-4v parts made using powder bed fusion additive manufacturing processes, Addit. Manuf. 1 (2014) 87–98.
- [51] R. Cunningham, C. Zhao, N. Parab, C. Kantzos, J. Pauza, K. Fezzaa, T. Sun, A.D. Rollett, Keyhole threshold and morphology in laser melting revealed by ultrahigh-speed x-ray imaging, Science 363 (6429) (2019) 849–852.
- [52] A. Matsunawa, J.-D. Kim, N. Seto, M. Mizutani, S. Katayama, Dynamics of keyhole and molten pool in laser welding, J. Laser Appl. 10 (6) (1998) 247–254.
- [53] C. Pei, D. Shi, H. Yuan, H. Li, Assessment of mechanical properties and fatigue performance of a selective laser melted nickel-base superalloy inconel 718, Mater. Sci. Eng. A 759 (2019) 278–287, https://doi.org/10.1016/j.msea.2019.05.007.
- [54] H. Gong, H. Gu, K. Zeng, J. Dilip, D. Pal, B. Stucker, D. Christiansen, J. Beuth, J.J. Lewandowski, Melt pool characterization for selective laser melting of ti-6al-4v pre-alloyed powder, Solid Freeform Fabrication Symposium, Austin (2014) 256–267.
- [55] L. Thijs, F. Verhaeghe, T. Craeghs, J. Van Humbeeck, J.-P. Kruth, A study of the microstructural evolution during selective laser melting of ti-6al-4v, Acta Mater. 58 (9) (2010) 3303–3312.
- [56] W.M. Tucho, V. Hansen, Characterization of slm-fabricated inconel 718 after solid solution and precipitation hardening heat treatments, J. Mater. Sci. 54 (1) (2019) 823–839.
- [57] P. Littlewood, T. Britton, A. Wilkinson, Geometrically necessary dislocation density distributions in ti-6al-4v deformed in tension, Acta Mater. 59 (16) (2011) 6489–6500, https://doi.org/10.1016/j.actamat.2011.07.016.
- [58] W.M. Tucho, P. Cuvillier, A. Sjolyst-Kverneland, V. Hansen, Microstructure and hardness studies of inconel 718 manufactured by selective laser melting before and after solution heat treatment, Mater. Sci. Eng. A 689 (2017) 220–232.
- [59] U.S. Bertoli, G. Guss, S. Wu, M.J. Matthews, J.M. Schoenung, In-situ characterization of laser-powder interaction and cooling rates through high-speed imaging of powder bed fusion additive manufacturing, Mater. Des. 135 (2017) 385–396.
- [60] H. Qi, M. Azer, A. Ritter, Studies of standard heat treatment effects on microstructure and mechanical properties of laser net shape manufactured inconel 718, Metall. Mater. Trans. A 40 (2009) 2410–2422, https://doi.org/10.1007/s11661-009-9949-3.
- [61] Y. Idell, L.E. Levine, A.J. Allen, F. Zhang, C.E. Campbell, G.B. Olson, J. Gong, D.R. Snyder, H.Z. Deutchman, Unexpected  $\delta$ -phase formation in additive-manufactured ni-based superalloy, JOM 68 (3) (2016) 950–959, https://doi.org/10.1007/s11837-015-1772-2.
- [62] F. Zupanič, T. Bonč ina, A. Križman, F. Tichelaar, Structure of continuously cast nibased superalloy inconel 713c, J. Alloys Compds. 329 (1–2) (2001) 290–297.
- [63] A. Bhambri, T. Kattamis, J. Morral, Cast microstructure of inconel 713c and its dependence on solidification variables, Metall. Trans. B 6 (4) (1975) 523–537.
- [64] S. Manikandan, D. Sivakumar, K.P. Rao, M. Kamaraj, Laves phase in alloy 718 fusion zone-microscopic and calorimetric studies, Mater. Charact. 100 (2015) 192–206.
- [65] H.Y. Wan, Z.J. Zhou, C.P. Li, G.F. Chen, G.P. Zhang, Effect of scanning strategy on mechanical properties of selective laser melted inconel 718, Mater. Sci. Eng. A 753 (2019) 42–48, https://doi.org/10.1016/j.msea.2019.03.007.
- [66] S. Sui, J. Chen, E. Fan, H. Yang, X. Lin, W. Huang, The influence of laves phases on the high-cycle fatigue behavior of laser additive manufactured inconel 718, Mater. Sci. Eng. A 695 (2017) 6–13.
- [67] H. Xiao, S. Li, X. Han, J. Mazumder, L. Song, Laves phase control of inconel 718 alloy using quasi-continuous-wave laser additive manufacturing, Mater. Des. 122 (2017) 330–339.
- [68] N.T. Aboulkhair, N.M. Everitt, I. Ashcroft, C. Tuck, Reducing porosity in alsi10 mg parts processed by selective laser melting, Addit. Manuf. 1 (2014) 77–86.
- [69] D. Deng, R.L. Peng, H. Brodin, J. Moverare, Microstructure and mechanical properties of inconel 718 produced by selective laser melting: sample orientation dependence and effects of post heat treatments, Mater. Sci. Eng. A 713 (2018) 294–306.

- [70] L. Parry, I. Ashcroft, R.D. Wildman, Understanding the effect of laser scan strategy on residual stress in selective laser melting through thermo-mechanical simulation, Addit. Manuf. 12 (2016) 1–15.
- [71] J. Grum, R. Šturm, A new experimental technique for measuring strain and residual stresses during a laser remelting process, J. Mater. Process. Technol. 147 (3) (2004) 351–358.
- [72] K. Wei, M. Lv, X. Zeng, Z. Xiao, G. Huang, M. Liu, J. Deng, Effect of laser remelting on deposition quality, residual stress, microstructure, and mechanical property of selective laser melting processed ti-5al-2.5 sn alloy, Mater. Charact. 150 (2019) 67–77.
- [73] W. Callister, D.G. Rethwisch, Fundamentals of Materials Science and Engineering, Wiley, London, UK, 2000.
- [74] X. Wang, K. Chou, Electron backscatter diffraction analysis of inconel 718 parts fabricated by selective laser melting additive manufacturing, JOM 69 (2) (2017) 402–408
- [75] M. Kirka, K. Unocic, N. Raghavan, F. Medina, R. Dehoff, S. Babu, Microstructure development in electron beam-melted inconel 718 and associated tensile properties, JOM 68 (3) (2016) 1012–1020.

- [76] Y. Tian, D. McAllister, H. Colijn, M. Mills, D. Farson, M. Nordin, S. Babu, Rationalization of microstructure heterogeneity in inconel 718 builds made by the direct laser additive manufacturing process, Metall. Mater. Trans. A 45 (10) (2014) 4470–4483.
- [77] N. Kouraytem, R.A. Chanut, D.S. Watring, T. Loveless, J. Varga, A.D. Spear, O.T. Kingstedt, Dynamic-loading behavior and anisotropic deformation of pre-and post-heat-treated in 718 fabricated by selective laser melting, Addit. Manuf. (2020) 101083
- [78] S. Beretta, S. Romano, A comparison of fatigue strength sensitivity to defects for materials manufactured by am or traditional processes, Int. J. Fatig. 94 (2017) 178–191.
- [79] B. Torries, A. Imandoust, S. Beretta, S. Shao, N. Shamsaei, Overview on microstructure-and defect-sensitive fatigue modeling of additively manufactured materials, JOM 70 (9) (2018) 1853–1862.
- [80] J. Zhao, M. Easton, M. Qian, M. Leary, M. Brandt, Effect of building direction on porosity and fatigue life of selective laser melted alsi12 mg alloy, Mater. Sci. Eng. A 729 (2018) 76–85.